

1
2
3
4
5
6
7
8
9
10
11
12
13
14
15
16
17
18
19
20
21
22
23
24
25
26
27

Future changes in Beijing haze events under different anthropogenic aerosol emission scenarios

Lixia Zhang^{1,2}, Laura J. Wilcox³, Nick J. Dunstone⁴, David J. Paynter⁵, Shuai Hu^{1,6},
Massimo Bollasina⁷, Donghuan Li⁹, Jonathan K. P. Shonk^{3,8}, and Liwei Zou¹

1 LASG, Institute of Atmospheric Physics, Chinese Academy of Sciences, Beijing, China

2 Collaborative Innovation Center on Forecast and Evaluation of Meteorological Disasters, Nanjing University of Information Science & Technology, Nanjing, 210044, China

3 National Centre for Atmospheric Science, Department of Meteorology, University of Reading, UK

4 Met Office Hadley Centre, FitzRoy Road, Exeter EX1 3PB, UK

5 NOAA/Geophysical Fluid Dynamics Laboratory, Princeton, New Jersey

6 University of Chinese Academy of Sciences, Beijing 100049, China

7 School of Geosciences, Grant Institute, University of Edinburgh, Edinburgh, UK

8 Now at: MetOffice@Reading, Department of Meteorology, University of Reading, UK

9 Key Laboratory of Water Cycle and Related Land Surface Processes, Institute of Geographic Sciences and Natural Resources Research, Chinese Academy of Sciences

Submitted to Atmospheric Chemistry and Physics

Revised on 17th Jan, 2021

Corresponding author: Dr. Lixia Zhang

LASG, Institute of Atmospheric Physics, Chinese Academy of Sciences, Beijing 100029, China

Phone: 86-10-8299-5456

Email: lixiazhang@mail.iap.ac.cn

28 **Abstract:** Air pollution is a major issue in China and one of the largest threats to public
29 health. We investigated future changes in atmospheric circulation patterns associated
30 with haze events in the Beijing region, and the severity of haze events during these
31 circulation conditions, from 2016 to 2050 under two different aerosol scenarios: a
32 maximum technically feasible aerosol reduction (MTFR) and a current legislation
33 aerosol scenario (CLE). In both cases greenhouse gas emissions follow the
34 Representative Concentration Pathway (RCP) 4.5. Under RCP4.5 with CLE aerosol the
35 frequency of circulation patterns associated with haze events increases due to a
36 weakening of the East Asian winter monsoon via increased sea level pressure over the
37 North Pacific. The rapid reduction in anthropogenic aerosol and precursor emissions in
38 MTFR further increases the frequency of circulation patterns associated with haze
39 events, due to further increases of the sea level pressure over the North Pacific and a
40 reduction in the intensity of the Siberian high. Even with the aggressive aerosol
41 reductions in MTFR periods of poor visibility, represented by above normal aerosol
42 optical depth (AOD), still occur in conjunction with haze-favorable atmospheric
43 circulation. However, the winter mean intensity of poor visibility decreases in MTFR,
44 so that haze events are less dangerous in this scenario by 2050 compared to CLE, and
45 relative to the current baseline. This study reveals the competing effects of aerosol
46 emission reductions on future haze events through their direct contribution to pollutant
47 source and their influence on the atmospheric circulation. A compound consideration
48 of these two impacts should be taken in future policy making.

49 **Key Words:** air-pollution, anthropogenic aerosol, atmospheric circulation, haze events

50

51 **1. Introduction**

52 The increases in aerosol and precursor emissions in China due to the rapid economic
53 development and urbanization in recent decades have caused more frequent and severe
54 haze events. Beijing and the surrounding area is the most polluted region in China (Niu
55 et al., 2010; Ding and Liu, 2014; An et al., 2019; Chen and Wang, 2015). Air pollution
56 has become one of the major issues in China, and the greatest threat to public health.
57 Since the implementation of the “Atmospheric Pollution Prevention and Control Action
58 Plan” in 2013 (China State Council, 2013), aerosol emissions have dramatically
59 decreased, with sulfur dioxide (SO₂) reduced by 59% in 2017 compared to 2013 (Zheng
60 et al., 2018). However, haze events have still occurred regularly in recent years, as, in
61 addition to being influenced by aerosol emissions, meteorological conditions, including
62 limited scavenging, dispersion and ventilation, have been found to play important roles
63 in the variation of air-quality in northern China (An et al., 2019; Pei et al., 2018; Cai et
64 al., 2017). Such events are typically associated with the occurrence of large-scale
65 atmospheric circulation patterns favoring the accumulation of pollutants (Chen and
66 Wang, 2015; Zhang et al., 2014). Locally, a strong temperature inversion in the lower
67 troposphere, weak surface winds, and subsiding air in the planetary boundary layer are
68 favorable for the development and persistence of haze events (Wu et al., 2017; Feng et
69 al., 2018). As anthropogenic aerosol has the potential to induce changes in the
70 atmospheric circulation, in addition to making a direct contribution to the chemical
71 composition of haze, it is crucial to understand how changes in aerosol emissions might

72 contribute to the frequency and intensity of haze events in future.

73 On interannual time scales, the East Asian winter monsoon (EAWM) is significantly
74 negatively correlated with aerosol concentrations in Beijing, due to the associated high
75 frequency of extreme anomalous southerly episodes in North China, a weakened East
76 Asian trough in the mid-troposphere and a northward shift of the East Asian jet stream
77 in the upper troposphere (Jeong and Park, 2017; Li et al., 2016; Pei et al., 2018). The
78 cold air process over Beijing is favorable for pollutant dispersion and transport outside
79 because of the accompanied large near-surface wind speed and deep mixing layer. A
80 low occurrence of cold air processes in the recent winters of 2013, 2014 and 2017 has
81 resulted in severe pollution (He et al., 2018). In the past decades, the weakening of the
82 EAWM was found to contribute to the increased frequency of haze events over North
83 China (Chen and Wang, 2015; An et al., 2019). Arctic sea ice extent also has been
84 linked to increased stability over eastern China, explaining 45%~67% of the interannual
85 to interdecadal variability of winter haze days over eastern China (Wang et al., 2015).
86 Overall, around half of the variability in the frequency of haze events in Beijing is
87 controlled by meteorological conditions, while both meteorological conditions and
88 aerosol emissions contribute to the intensity (Pei et al., 2020). Internal climate
89 variability has contributed to the rapid increase of early winter haze days in North China
90 since 2010 (Zhang et al., 2020).

91 Anthropogenic forcing, estimated by using large ensemble runs with and without
92 anthropogenic forcings, has also increased the probability of the atmospheric patterns

93 conducive to severe haze in Beijing by weakening the EAWM (Li et al., 2018).
94 Projections based on Coupled Model Intercomparison Project Phase 5 (CMIP5) models
95 showed that weather conditions conducive to haze events in Beijing will increase with
96 global warming due to an increased occurrence of stagnation days in response to both
97 accelerated Arctic ice melting (Cai et al., 2017; Liu et al., 2019a) and a continued
98 weakening of EAWM (Hori et al., 2006; Pei and Yan, 2018; Liu et al., 2019a). If there
99 is no change in aerosol emission in future, increased stagnation days and decreased light
100 precipitation days associated with global warming would also cause an increase in air
101 pollution days in eastern China (Chen et al., 2019). Regional climate model simulations
102 under the RCP4.5 scenario showed that the air environment carrying capacity, a
103 combined metric measuring the capacity of the atmosphere to transport and dilute
104 pollutants, tends to decrease in the 21st century across China (Han et al., 2017).
105 However, there is a large uncertainty in future aerosol emission pathways, with
106 uncertainty around the sign of the change in global emission rate, as well as choice of
107 haze index, and internal climate variability (Scannell et al., 2019; Callahan et al., 2019;
108 Callahan and Mankin, 2020). Furthermore, changes in aerosol emission may influence
109 the haze-favorable atmospheric circulation, in addition to their role in haze composition.
110 The interplay between the role of aerosol as a constituent of haze, and as a potential
111 driver of changes in the circulation patterns conducive to haze, have yet to be explored.
112 If the rapid reductions in aerosol and precursor emissions currently underway in China
113 continue in future, understanding the balance between the different influences of

114 anthropogenic aerosol forcing on haze events is a key question. Typically,
115 anthropogenic aerosol (AA) and greenhouse gases (GHGs) both vary in the future (e.g.
116 those following the RCPs or Shared Socioeconomic Pathways), which can make their
117 relative contributions difficult to determine. In this work, we examine future scenarios
118 with the same GHGs emission pathway but different aerosol pathways in order to
119 separate the role of AA forcing. We address the following two questions: 1) Do the
120 atmospheric conditions conducive to haze events change differently under different AA
121 scenarios? 2) If so, how AA forcing modulate the frequency of haze-favorable
122 circulation and the severity of the haze events change?

123 The remainder of the paper is organized as follows: we briefly introduce the experiment
124 design and methods in Section 2, and show the atmospheric circulation patterns
125 conducive to Beijing haze events in Section 3. Projected Beijing haze events under two
126 different aerosol emissions and the underlying mechanism of projected circulation
127 changes will be given in Section 4. We will finally provide the summary and discussion
128 in Section 5.

129 **2. Experiments and methods**

130 **2.1 Data and experiment design**

131 We use observed daily visibility, relative humidity and wind speed from 1974 to 2013
132 from the National Climatic Data Center (NCDC) Global Surface Summary of the Day
133 (GSOD) database (Fig.S1a). Haze days are defined as days with daily visibility less

134 than 10km, relative humidity less than 90% and surface wind speed less than 7 m s^{-1}
135 (Chen and Wang, 2015). The observed haze occurrence is the number of haze days, and
136 observed haze intensity is defined as the minimum 3-day consecutive visibility
137 (VN3day). Spatial distributions of winter mean haze occurrence and VN3day are shown
138 in Fig.S1b-c. Data from the Japanese 55-year Reanalysis (JRA55; Kobayashi et al.,
139 2015) dataset for the period 1958-2013 are used in this study to evaluate the model
140 representations of the present-day climate. The variations of haze index derived from
141 JRA-55 are highly consistent with those from NCEP-NCAR reanalysis (not shown).
142 We only use JRA-55 in this study.

143 Simulations with the Met Office Unified Model (Global Coupled configuration 2)
144 HadGEM3-GC2 (Williams et al., 2015) and the NOAA Geophysical Fluid Dynamics
145 Laboratory (GFDL) Climate Model version 3 (GFDL-CM3, Donner et al., 2011;
146 Griffies et al., 2011) are used to investigate the impact of different aerosol forcing
147 scenarios. HadGEM3-GC2 is run with a horizontal resolution of N216 (~60 km) in the
148 atmosphere, and $\frac{1}{4}^\circ$ in the ocean. GFDL-CM3 has a horizontal resolution of ~200 km
149 in the atmosphere and 1° in the ocean. Both models include a representation of aerosol-
150 cloud interactions (Ming et al., 2006; Bellouin et al., 2011).

151 Three sets of experiments were carried out with each model (Table S1): a historical
152 experiment from 1965 to 2014 and two experiments for the future (2016-2050). In the
153 historical experiment, greenhouse gases and anthropogenic aerosol and precursor
154 emissions are taken from CMIP5 (Lamarque et al., 2010; Taylor et al., 2012). The future

155 experiments have common GHG emissions following the RCP4.5 scenario, but
156 different aerosol emission pathways. The aerosol pathways are the current legislation
157 emissions (CLE) and the maximum technically feasible reduction (MTFR) taken from
158 the ECLIPSE V5a global emission dataset (Amann et al., 2015,
159 <https://iiasa.ac.at/web/home/research/researchPrograms/air/ECLIPSEv5a.html>). In
160 CLE, anthropogenic aerosol emissions are assumed to evolve following the current
161 legislation, resulting in a moderate global increase by 2050. In contrast, MTFR assumes
162 a full implementation of the most advanced technology presently available to reduce
163 aerosol emissions by 2030, which results in their rapid global decrease over this period.
164 The regional changes in AA for His, CLE and MTFR can be found in Scannell et al.
165 (2019) and Luo et al. (2020).

166 We use 1980-2004 as a baseline (His), 2016-2050 as the future period, and display
167 anomalies between the two. Compared with His, CLE shows a dramatic increase in SO₂
168 over Asia, with peak values over India (not shown) and eastern China (Fig.S2a). MTFR
169 has similar changes over Europe to CLE, negligible changes over India (not shown),
170 and a dipole over China, with a weak increase to the north and a decrease to the south
171 (Fig.S2b). Thus, a dramatic decrease in SO₂ in MTFR relative to CLE is seen over the
172 whole Asian continent, particularly over the Beijing region (Fig. S2c).

173 **2.2 Haze weather index and East Asian winter monsoon index**

174 We focus on haze events during the winter (December-February) around Beijing where
175 Chinese haze events are most frequent and severe (Niu et al., 2010; Chen and Wang,

176 2015). In this study, we use the haze weather index (HWI) proposed by Cai et al. (2017)
177 as it has also been shown to have a strong relationship with PM_{2.5} concentrations in
178 Beijing.

179 The HWI comprises three constituent terms representing the vertical temperature
180 gradient in the troposphere (ΔT), the 850-hPa meridional wind (V_{850}), and the north—
181 south shear in the 500-hPa zonal wind (U_{500}) (see boxes and lines in Fig.1). ΔT is
182 calculated as the difference between the 850 hPa temperature averaged over (32.5°–
183 45°N, 112.5°–132.5°E) and the 250-hPa temperature averaged over (37.5°–45°N,
184 122.5°–137.5°E). V_{850} is the 850hPa meridional wind averaged over the broader
185 Beijing region (30°–47.5°N, 115°–130°E), and U_{500} is a latitudinal difference between
186 the 500-hPa zonal wind averaged over a region to the north of Beijing (42.5°–52.5° N,
187 110°–137.5°E) and a region to the south (27.5°–37.5°N, 110°–137.5°E). Each of the
188 three terms is normalized by their standard deviation over the reference period (here
189 1980-2004). The three variables are added together to create the HWI, which is then
190 normalized again by its standard deviation over the reference period. A positive HWI
191 represents conditions that are unfavorable to air-pollutant dispersion, and days with
192 $HWI > 0$ are regarded as “haze events”. The HWI defined by Cai et al. (2017) made use
193 of daily data. Due to unavailability of model data at daily resolution, we instead used
194 monthly data. The reliability of using HWI calculated from monthly mean variables
195 will be discussed in Section 3 based on reanalysis.

196 The strength of the EAWM is quantified using the index defined by Wang and Chen
197 (2014). This index takes into account both the east-west and the north-south pressure
198 gradients and is defined as:

$$199 \quad \text{EAWM} = (2 \times \text{SLP}_1 - \text{SLP}_2 - \text{SLP}_3) / 2$$

200 Where SLP_1 , SLP_2 and SLP_3 represent normalized sea level pressure (SLP) averaged
201 over Siberia (40-60°N, 70-120°E), the North Pacific (30-50°N, 140°E-170°W) and the
202 Maritime Continent (20°S-10°N, 110-160°E), respectively (see the boxes in Fig.S3).
203 The three components are converted to anomalies and normalized by their standard
204 deviation over the reference period (here 1980-2004). As the EAWM is directly linked
205 to the occurrence of favorable conditions for haze in Beijing (Pei et al., 2018; Liu et al.,
206 2019b; Hori et al., 2006), we therefore use this index as an additional metric to assess
207 the potential changes in future haze events under the CLE and MTFR scenarios, and
208 confirm the robustness of the changes indicated by HWI.

209 **2.3 Significance test**

210 To test whether projected winter mean HWI change and frequency of month with
211 $\text{HWI} \geq 1$ are statistically significant, we estimated internal variability by performing
212 bootstrapped samples. This resampling-based procedure involves three steps. First, we
213 randomly select 75-month (135-month), i.e. 25-yr (45-yr) winters, from His
214 (projections), and calculate the mean HWI change of the 75-month relative to His or
215 frequency of month with $\text{HWI} \geq 1$ of the 75-month. The 75-month and 135-month are

216 selected to mimic any 25-yr in the period 1980-2004 and 45-yr in 2016–2050,
217 respectively; We repeat the first step 2000 times, and the 2000 bootstrapped samples
218 can be viewed as internal variability of His or future projections. We then compare the
219 results of model ensemble mean with the 2000 bootstrapped samples. If it falls outside
220 the top 5% of the distribution, we then claim that the projected changes in mean HWI
221 or frequency of month with $\text{HWI} \geq 1$ are statistically significant at the 5% level and
222 beyond the variability of internal variability. We also employed a two-sample
223 Kolmogorov-Smirnov test to determine if the probability density function (PDF)
224 distributions are significantly different (Chakravarti et al., 1967).

225 3. **Favorable climatic conditions for Beijing haze events in reanalysis**

226 The circulation anomalies averaged over the days with daily $\text{HWI} > 0$ are shown in
227 Fig.1a, c, e. The vertical temperature profile shows warmer air at the lower to mid-
228 levels, centered around 850hPa and cold anomalies aloft 250hPa (Fig.1a). Thus, the
229 atmosphere is stable, unfavorable for the vertical dispersion of pollutants. At the mid-
230 latitude (500hPa), we see northward shifted mid-level westerly jets (Fig.1c). The
231 weakened westerly winds along 30°N inhibit the horizontal dispersion of pollutants in
232 Beijing. At the lower-level, the anomalous southerly winds at 850hPa along the East
233 Asian coast lead to a reduction in the prevailing surface cold northerlies in winter
234 (Fig.1e). This reduction favors warmer conditions at lower levels and increased
235 moisture over Beijing, thus increasing the likelihood of haze formation and
236 maintenance.

237 The HWI was defined based on daily data. Due to limitations in data availability, we
238 instead used monthly data to calculate HWI. To determine the reliability of this
239 approach, we first examined the relationship between the magnitude of HWI calculated
240 from monthly data (HWI-month) and the number of days with daily HWI (HWI-daily) >
241 0 in the JRA-55 reanalysis during the period 1958-2013 (Fig. 2a-b). The variability of
242 HWI-month is highly consistent with that of number of days with HWI-daily>0 ($r =$
243 0.97). When HWI-month is greater than 0, about 50% days in that month are recognized
244 with HWI-daily>0, and up to 62% days with HWI-daily >0 when HWI-month ≥ 1 . In
245 this study, we define favorable climatic conditions of haze events around Beijing as a
246 month where HWI-month ≥ 1 .

247 We also checked the observed winter haze occurrence and intensity (VN3day)
248 anomalies when HWI-month ≥ 1 . More haze occurrence and reduced visibility are
249 observed over North China, indicating the reliability of using HWI-month ≥ 1 as a proxy
250 of the favorable climatic conditions for the haze events in Beijing and the surrounding
251 region. The selection of a higher threshold of HWI-month (e.g. 1.5) does not make a
252 great difference to our results (not shown). The circulation anomalies averaged over
253 HWI-month ≥ 1 (Fig. 1b, d, f) and HWI-daily > 0 (Fig. 1a, c, e) are also consistent with
254 each other, except that the anomalies for HWI-month ≥ 1 are weaker, as would be
255 expected. The spatial and temporal consistency of HWI anomalies calculated from
256 monthly and daily data confirms the suitability of our use of monthly data to explore
257 changes in the frequency of Beijing haze events associated circulation. In the following

258 sections, we will use the term HWI to indicate HWI-month for brevity.

259 **4. Changes in Beijing haze events under two AA emission scenarios**

260 *4.1 Changes in the frequency of haze-favorable circulation patterns*

261 Both HadGEM3-GC2 and GFDL-CM3 well simulate the key spatial features of the
262 large-scale atmospheric circulation in winter, when compared to JRA-55 for 1980-2004
263 (Fig.S4). Key features include the westerly jet along 30°N, the East Asian trough, and
264 northerly winds along the East Asian coast, which are caused by the zonal thermal
265 contrast and subsequent pressure gradient between the North Pacific and the Eurasian
266 continent. The models can also reliably capture the vertical temperature difference, the
267 weaker East Asian trough and the anomalous 850-hPa southerly winds associated with
268 haze events (Fig.S5 and Fig.1). The good performance of HadGEM3-GC2 and GFDL-
269 CM3 in simulating the winter monsoon and haze-favorable circulation justifies the use
270 of these two models to estimate HWI changes.

271 There is a large interannual variability in HWI, and no significant trend in HWI either
272 in His, CLE or MTFR (not shown). However, the two models both show an increase in
273 the mean HWI with no consistent change in the standard deviation (Fig.3a, c). The
274 mean HWI in His (1980-2004), CLE (2016-2050) and MTFR (2016-2050) is 0.00, 0.39,
275 and 0.65 in HadGEM3-GC2. In GFDL-CM3 it is 0, 0.46, and 0.60. There is a slight
276 increase in the standard deviation of HWI in HadGEM3-GC2 from His (1.0) and CLE
277 (1.0) to MTFR (1.06), while no change is seen in GFDL-CM3. The occurrence of

278 positive HWI in CLE and MTFR increases relative to His in both models. In both
279 models, the PDF distributions of HWI in His and CLE are significantly different at the
280 1% level using a Kolmogorov-Smirnov test. For the distributions of HWI in CLE and
281 MTFR, they are also significantly different at the 1% level in HadGEM3-GC2, but not
282 in GFDL-CM3. The changes in the frequency of different HWI can be found from the
283 cumulative distribution function (CDF) of HWI (Fig.3b, d). The frequency of $HWI \geq 1$
284 for His, CLE and MTFR is ~18% (16%), 28% (31%), and 34% (37%) in HadGEM3-
285 GC2 (GFDL-CM3), respectively. If AA emissions follow the CLE scenario, the
286 frequency of month with $HWI \geq 1$ will increase by 10% and 15% in HadGEM3-GC2
287 and GFDL-CM3, respectively. The rapid reduction in AA emissions in MTFR
288 contributes to an extra 6% increase in HWI relative to CLE in both models.

289 We used a bootstrapping approach to test whether the mean winter HWI changes and
290 to determine whether the frequency of month with $HWI \geq 1$ among His, CLE and MTFR
291 are significantly different from each other (Fig.4). The difference in mean HWI between
292 CLE vs His, MTFR vs His, and CLE vs MTFR, are also statistically significant at the
293 5% level in both models (Fig.4a-b). The frequency of month with $HWI \geq 1$ in CLE and
294 MTFR are both statistically different from that in His in the two models, while only in
295 HadGEM3-GC2 simulations is the frequency in MTFR statistically significant from
296 that in CLE at the 5% level (Fig. 4c-d).

297 An examination of the future changes in each component of the HWI is shown in Fig.S6.
298 The shift of HWI towards more positive values from His to CLE, with a larger shift in

299 MTFR relative to His, is found in all three components except that in V850 in GFDL-
300 CM3. The distributions of all the component terms of the His are statistically different
301 from CLE and from MTFR at the 5% level in both models by using a two-sample
302 Kolmogorov-Smirnov test, while the distributions in CLE and MTFR are significantly
303 different in HadGEM3-GC2 only, consistent with our conclusion based on the
304 bootstrapping approach. The changes of the three components of HWI demonstrate the
305 atmospheric conditions favoring haze events all become more likely with global
306 warming, and that future AA reductions may further increase their likelihood.

307 *4.2 Possible mechanism for atmospheric circulation changes*

308 To investigate the mechanism underlying these changes in Beijing haze-favorable
309 circulation frequency, we present the changes in the vertical temperature profile, and
310 spatial patterns of 850-hPa and 500-hPa winds in Figs.5-7. The lower- and mid-
311 troposphere displays an incremental warming from His to MTFR compared to the upper
312 levels in both models. The peak warming is at 700 hPa and over 120°-130°E.
313 Conversely, both models simulate an upper-tropospheric cooling at 250 hPa in CLE
314 compared to His, albeit of smaller magnitude than the warming below (Fig.S7).
315 However, the 250 hPa temperature changes between MTFR and CLE differ in the two
316 models (Fig.5b, d and Fig.S7g-h). Thus, the increase in tropospheric stability in MTFR
317 relative to CLE is mainly driven by low-level warming.

318 Following the CLE aerosol pathway, both HadGEM3-GC2 and GFDL-CM3 project an
319 anomalous 850-hPa cyclonic circulation over the northwestern Pacific (0-20°N, 120-

320 180°E) relative to His, and an anticyclonic anomaly to its north (20-50°N, 120-180°E)
321 (Fig.6a-b). This pattern bears some resemblance to the anomalous circulation
322 associated with a positive phase of the Arctic Oscillation, which may be due to melting
323 Arctic sea ice (Shindell et al., 1999; Fyfe et al., 1999; Wang et al., 2020). The southerly
324 wind anomalies over eastern China, on the western flank of the anomalous anticyclone,
325 act to weaken the East Asian winter monsoon and reduce its low-level winds, making
326 conditions favorable for air-pollutant transport from south to north and air-pollutant
327 accumulation more likely. With the addition of rapid AA reductions following MTFR,
328 the 850-hPa circulation anomalies are reinforced further (Fig6.c-d), especially in
329 HadGEM3-GC2, which simulates much stronger southerly wind anomalies along the
330 East Asian coast. GFDL-CM3 shows similar anomalies over the North Pacific in CLE
331 vs His and MTFR vs His, but distinct responses over China (Fig.6d), which likely
332 explains why GFDL-CM3 does not simulate the further shift in HWI seen in
333 HadGEM3-GC2 between CLE and MTFR (Fig.S6c, f). A northeasterly anomaly is seen
334 over southeast China in GFDL-CM3 in both CLE relative to His and MTFR relative to
335 CLE. However, the onshore flow over Beijing seen in CLE relative to His, which is
336 likely to be a key contributor to an increase in haze weather events, is not enhanced
337 further by the rapid aerosol reductions in MTFR (Fig. 6d).

338 At 500 hPa, a northward shift of the westerly jet stream is projected in CLE relative to
339 the current baseline, with significant positive zonal wind anomalies along 50°N and
340 negative anomalies along 30°N in both models (Fig.7a-b). This shift is consistent with

341 the increase in the meridional temperature gradient over the North Pacific (Fig.S7).
342 Thus, the East Asian winter trough is weakened, bringing less cold and dry air to the
343 Beijing area, and favoring the formation and maintenance of haze events. The
344 reductions in AA emissions in MTFR relative to CLE significantly strengthen the
345 above-mentioned circulation anomalies at 500 hPa in both models (Fig 7c,d), and
346 further increase the frequency of positive U500 differences in the regions used to
347 calculate the HWI, as seen in Fig.7c-d. The changes in 500-hPa zonal winds are
348 consistent between the two models, demonstrating the robustness of the results.

349 The changes in the three components of HWI in CLE relative to His indicate a
350 weakened EAWM with increased GHGs, with reductions in AA emissions further
351 amplifying this effect and increasing the frequency of large-scale circulation conditions
352 conducive to Beijing haze events. To explore how the EAWM circulation responds to
353 reductions in AA emissions, we show surface temperature and sea level pressure
354 changes in MTFR relative to CLE (Fig. 8). Reduced AA emissions generally amplify
355 the impact of greenhouse gases, with more warming over the Arctic, the Eurasian
356 continent and Northwestern Pacific. Thus, the Aleutian low is further weakened in
357 MTFR. In addition, more warming over the Eurasian continent and Northwestern
358 Pacific leads to a SLP decrease over Siberia and the northwestern Pacific, respectively.

359 The main difference between the two models is found from the SLP changes over the
360 Eurasian continent in the mid-latitudes, where large negative SLP anomalies are
361 presented in HadGEM3-GC2 while there are no changes in GFDL-CM3. This may lead

362 to the less westward shift of the North Pacific anomalous anticyclonic circulation in
363 GFDL-CM3 in Fig.6d.

364 The PDF distributions of EAWM, using the Wang and Chen (2014) index, in His, CLE
365 and MTFR are shown in Fig.8e-f. The EAWM weakens in CLE compared to His (blue
366 and grey lines in Fig.8e-f), mainly due to increased SLP over the North Pacific (SLP₂,
367 Fig.S8 b, e), with no systematic changes in SLP over Siberia (SLP₁) and the Maritime
368 continent (SLP₃) (Fig.S8a, d, and Fig.S8c, f). The rapid AA reductions in MTFR cause
369 the SLP over Siberia to decrease consistently in both models alongside a further
370 increase in SLP₂. The changes in SLP₂ (SLP₁) are statistically significant at the 5%
371 (10%) level in both models tested by performing bootstrapped samples (not shown).
372 This further weakens the east-west contrast, leading to a weaker EAWM in MTFR
373 relative to CLE, consistent with the differences between CLE and His and between
374 MTFR and CLE seen in the HWI. The response of SLP over the Maritime Continent
375 (SLP₃) to AA reductions differs between the two models, indicating a large uncertainty
376 in the SLP₃ changes. Thus, the AA forcing reduction predominantly weakens the
377 EAWM through reducing the zonal thermal contrast.

378 ***4.3 Changes in haze intensity associated with favoring circulation***

379 Occurrence of a haze event requires stagnant atmospheric conditions, and also a
380 pollution source. Although future aerosol reductions may cause further increases in the
381 frequency of atmospheric circulation patterns currently linked with haze events, such
382 events may become less severe in the absence of large aerosol emissions. In this section,

383 we will examine the projected changes in the intensity of Beijing haze events using the
384 aerosol optical depth (AOD) at 550nm as a metric for aerosol-induced poor visibility.
385 The simulated baseline winter mean AOD around Beijing area is shown in Fig.9a, c. To
386 account for model differences in historical AOD, we used the ratio of AOD at 550nm
387 (hereafter AOD_ratio) relative to a baseline winter mean to represent the air-pollution
388 severity. When AOD_ratio is greater than 1.0, the air-pollution intensity is higher than
389 baseline climate mean. HadGEM3-GC2 and GFDL-CM3 both simulate elevated AOD
390 around Beijing when circulation conditions are favorable ($HWI \geq 1$) (Fig.9 b, d): 1.4 and
391 1.3 times of the baseline climate mean in HadGEM3-GC2 and GFDL-CM3 respectively.
392 Aerosol and precursor emission increases under CLE (Fig. S1) result in a significant
393 increase in climate winter mean AOD around Beijing (reaching 1.2 times in HadGEM3-
394 GC2 and 1.05 times in GFDL-CM3), while climate mean AOD in MTFR decreases to
395 0.93 of the baseline climate mean around Beijing in the two models due to aerosol
396 emissions reduction (Fig.S9).

397 To check whether poor air quality events still occur even with reduced future aerosol
398 emissions, we show the projected AOD_ratio with $HWI \geq 1$ in Fig.10. In CLE, when
399 $HWI \geq 1$ AOD_ratio is elevated compared to the baseline climatology, to 1.6 times of
400 the baseline winter mean in HadGEM3-GC2 and 1.1 times that in GFDL-CM3 (Fig.10
401 a, c). It is consistent with the increase in aerosol loadings and climate mean AOD in
402 CLE (Fig.S2a and Fig.S9a-b). However, in MTFR, when $HWI \geq 1$, AOD is also higher
403 than the baseline climatology, albeit with a decrease in climate mean AOD in MTFR

404 (Fig.10 b,d). So, even with the aggressive aerosol reductions in MTFR, periods of poor
405 visibility still occur in conjunction with atmospheric circulation patterns associated
406 with haze in the current climate.

407 We calculated the PDF distributions of AOD_ratio surrounding the Beijing region (box
408 region in Fig.2) in the months with $HWI \geq 1$ in His, CLE and MTFR (Fig.11). In His,
409 the area-averaged AOD_ratio around the Beijing region when $HWI \geq 1$ is elevated to
410 1.34 (1.26) times of the baseline climate mean in HadGEM-GC2 (GFDL-CM3)
411 (Fig11.a-b). The change in AOD_ratio with $HWI \geq 1$ under CLE relative to His is
412 different between the two models. It increases to 1.51 in HadGEM3-GC2 but decreases
413 to 1.13 in GFDL-GC3. As expected, the AOD_ratio with $HWI \geq 1$ in MTFR reduces in
414 both models due to the dramatic reduction in anthropogenic aerosols. Thus, the mean
415 air-pollution intensity with the favorable circulation conditions for haze under MTFR
416 will be greatly relieved.

417 This reduction in GFDL-CM3 under CLE relative to His may be a reflection of the
418 model's bias. In JRA-55 when $HWI \geq 1$ there are southerly anomalies over southern
419 China. However, in the baseline in GFDL-CM3 there is an anomalous cyclonic
420 circulation, which may act to reduce pollutant accumulation in Beijing (Fig.S5). As
421 shown in Fig. 6b, d, this anomaly is strengthened in both CLE and MTFR.

422 To check whether extreme air pollution events would still occur, the probability of
423 AOD_ratio when $HWI \geq 1$ in the three scenarios are examined (Fig.11b, d). In this study,
424 the mean AOD_ratio across all months when $HWI \geq 1$ in His is regarded as the winter

425 mean intensity of baseline haze events, i.e., the grey vertical lines in Fig.11a, c. The
426 probability of haze event intensity exceeding this threshold is about 42% and 34% in
427 HadGEM3-GC2 and GFDL-CM3, respectively (Fig.11b, d). Under CLE, it increases
428 to 52% in HadGEM3-GC2 while decreases to 28% in GFDL-CM3, consistent with
429 Fig.10a, c. In MTFR, lower probability is projected in both models, 24% in HadGEM-
430 GC2, and 21% in GFDL-CM3. This demonstrates that severe events (i.e., higher
431 AOD_ratio) would still happen in MTFR albeit with dramatic reduction in
432 anthropogenic aerosol, even though the mean intensity of haze events themselves will
433 become less dangerous if aerosol emissions are reduced.

434 **5 Summary and discussion**

435 During recent decades, with rapid increases in aerosol and precursor emissions in China,
436 air pollution has become one of the greatest threats to public health. Anthropogenic
437 aerosol contributes not only to the chemical composition of haze, but also has the
438 potential to modulate atmospheric circulation changes. Thus, this paper aims to
439 quantify the incidences of haze events in a future climate and the influence of aerosol
440 mitigation efforts. In this study, we examined the changes in the frequency of
441 atmospheric conditions conducive to haze events around Beijing region, and the
442 changes in aerosol optical depth (AOD) during these circulation conditions through the
443 mid-21st century under two different anthropogenic aerosol scenarios using two climate
444 models, HadGEM3-GC2 and GFDL-CM3. We also investigated the mechanism for the
445 changes in the large-scale atmospheric circulation.

446 We found that future greenhouse gases (GHG) increases and anthropogenic aerosol
447 (AA) increases following a current legislation aerosol scenario (CLE) will increase the
448 frequency of haze-favorable atmospheric circulation conditions surrounding the Beijing
449 region. The frequency of haze weather index ($\text{HWI} \geq 1$) derived from monthly data in
450 HadGEM3-GC2 (GFDL-GCM3) increases from ~18% (16%) at baseline to ~28%
451 (31%) for 2016-2050 under the CLE scenario. By comparing the scenario with a
452 maximum technically feasible aerosol reduction (MTFR), which has the same GHG
453 increases but rapid aerosol reductions, we show that future aerosol reductions may
454 further amplify the increase in the frequency of such circulation patterns. Rapid
455 reductions in AA emissions in MTFR contribute to an extra ~6% increase in $\text{HWI} \geq 1$ in
456 two models.

457 The increase in haze frequency in CLE is mainly due to a weakening of the East Asian
458 winter monsoon, warming of the lower troposphere, and weakening of the East Asian
459 trough, which is likely to be predominantly driven by the GHG increases. Reduced AA
460 forcing in MTFR could further enhance the above circulation anomalies and amplify
461 the impact of greenhouse gases. Because the AA emission reductions in MTFR relative
462 to CLE mainly occur over continental Asia, the Asian landmass receives more
463 shortwave radiation, leading to a warmer surface temperature there. This leads to a
464 weaker Siberian high, and further contributes to the weakening of the East Asian winter
465 monsoon in MTFR.

466 The analysis of haze intensity based on AOD at 550 nm shows that visibility with

467 HWI \geq 1 is always lower than the baseline winter mean under both CLE and MTFR.
468 With more reduction in aerosol emissions following the MTFR, the mean intensity of
469 haze events in the haze-favorable atmospheric circulation will become less dangerous
470 compared to that in His and CLE in both models. Meanwhile, the probability of haze
471 event with intensity exceeding the baseline mean also decrease in MTFR,
472 demonstrating that severe haze events would also occur in MTFR.

473 This paper reveals the competing impacts of AA emission reductions on haze-favorable
474 circulation and haze intensity surrounding Beijing. AA reductions cause an increased
475 frequency of atmospheric circulation patterns conducive to haze events, but a reduction
476 in the haze intensity when these circulation patterns do occur. We found that the
477 capability of the models in representing haze-favorable large-scale circulations may
478 impact the simulation of AOD, which introduces further uncertainties in future
479 projection of AOD. Model evaluation on haze-favorable circulation and associated
480 AOD is necessary for future projection. Our results are consistent with previous studies
481 that global warming, and more reduction in aerosol forcing caused extra warming, will
482 make haze-favorable conditions around Beijing area more frequent (Callahan and
483 Markin, 2020). But internal variability may not be fully sampled because of limited
484 number of realization and models used in this study. In the future, single forcing
485 experiments and large ensemble simulations are useful ways to confirm the relative role
486 of greenhouse gases and anthropogenic aerosol forcing on haze events.

487 **Code/Data availability:** The National Climatic Data Center (NCDC) Global Surface

488 Summary of the Day (GSOD) database can be downloaded from the GSOD website
489 (<https://catalog.data.gov/dataset/global-surface-summary-of-the-day-gsod>). The JRA-
490 55 reanalysis data can be freely downloaded from the rda.ucar.edu website
491 (<https://rda.ucar.edu/datasets/ds628.0/>). Requests for outputs of the His, CLE and
492 MTRF experiments, or any questions regarding the data, can be directed to the
493 corresponding author, L Zhang (lixiazhang@mail.iap.ac.cn).

494 **Author contribution:** L Zhang designed and wrote the manuscript with support from
495 all authors. LJW and MAB helped design the analysis and supervised the work. NJD
496 and DJP ran the simulations. Shuai Hu analyzed the reanalysis data. Donghuan Li and
497 Liwei Zou contributed to the validation of observational metrics.

498 **Competing interests:** The authors declare that they have no conflict of interest.

499 **Acknowledgement:** This work was jointly supported by the Ministry of Science and
500 Technology of China under Grant 2018YFA0606501 and the National Natural Science
501 Foundation of China under grant No. 41675076. LJW, MAB and JKPS were supported
502 by the UK-China Research & Innovation Partnership Fund through the Met Office
503 Climate Science for Service Partnership (CSSP) China as part of the Newton Fund.
504 Liwei Zou is supported by National Natural Science Foundation of China under grant
505 No. 41830966.

506 **Reference:**

507 Amann M., I. Bertok, J. Borken-Kleefeld, J. Cofala, C. Heyes, L. Hoglund-Isaksson, G.
508 Kiesewetter, Z. Klimont, W. Schöpp, N. Vellinga, W. Winiwarter: Adjusted

509 historic emission data, projections, and optimized emission reduction targets for
510 2030 – A comparison with COM data 2013. Part A: Results for EU-28. TSAP
511 Report #16A, version 1.1. IIASA, Laxenburg, Austria, 2015.

512 An Z., R. Huang, R. Zhang, X. Tie, G. Li, J. Cao, W. Zhou, Z. Shi, Y. Han, Z. Gu, Y.
513 Ji: Severe haze in northern China: A synergy of anthropogenic emissions and
514 atmospheric processes. *Proceedings of the National Academy of Sciences of the*
515 *United States of America*, 116 (18), 8657–8666,
516 <https://doi.org/10.1073/pnas.1900125116>, 2019.

517 Bellouin, N., J. Rae, A. Jones, C. Johnson, J. Haywood, and O. Boucher: Aerosol
518 forcing in the Climate Model Intercomparison Project (CMIP5) simulations by
519 HadGEM2-ES and the role of ammonium nitrate, *J. Geophys. Res.*, 116, D20206,
520 [doi:10.1029/2011JD016074](https://doi.org/10.1029/2011JD016074), 2011.

521 Cai W J, K. Li, H. Liao, H. Wang, L. Wu: Weather conditions conducive to Beijing
522 severe haze more frequent under climate change, *Nat. Clim. Change*. 7, 257–62,
523 2017.

524 Callahan, C. W., and Mankin, J. S.: The influence of internal climate variability on
525 projections of synoptically driven Beijing haze. *Geophysical Research Letters*, 46,
526 e2020GL088548. <https://doi.org/10.1029/2020GL088548>, 2020.

527 Callahan, C. W., Schnell, J. L., and Horton, D. E.: Multi-index attribution of extreme
528 winter air quality in Beijing, China. *Journal of Geophysical Research:*
529 *Atmospheres*, 124, 4567–4583. <https://doi.org/10.1029/2018JD029738>, 2019.

530 Chakravarti, Laha, and Roy: *Handbook of Methods of Applied Statistics, Volume I*,
531 John Wiley and Sons, 392-394, 1967.

532 Chen, H.P., H. J., Wang: Haze Days in North China and the associated atmospheric
533 circulations based on daily visibility data from 1960 to 2012. *J. Geophys. Res.*
534 *Atmos.*, 120, 5895–5909, <https://doi.org/10.1002/2015JD023225>, 2015.

535 Chen H., H. Wang, J. Sun, Y. Xu, Z. Yin: Anthropogenic fine particulate matter
536 pollution will be exacerbated in eastern China due to 21st century GHG warming.

537 Atmospheric Chemistry and Physics, 19, 233–243, [https://doi.org/10.5194/acp-](https://doi.org/10.5194/acp-19-233-2019)
538 19-233-2019, 2019.

539 China State Council: Action Plan on Prevention and Control of Air Pollution, China
540 State Council, Beijing, China, [http://www.gov.cn/zwggk/2013-](http://www.gov.cn/zwggk/2013-09/12/content_2486773.htm)
541 09/12/content_2486773.htm (last access: 17 January 2021), 2013.

542 Ding, Y. H. and Liu, Y. J.: Analysis of long-term variations of fog and haze in China
543 in recent 50 years and their relations with atmospheric humidity, *Sci. China Earth*
544 *Sci.*, 57, 36–46, 2014.

545 Donner, L. J., B. L. Wyman, R. S. Hemler, L. W. Horowitz, Y. Ming et al.: The
546 dynamical core, physical parameterizations, and basic simulation characteristics
547 of the atmospheric component of the GFDL global coupled model CM3. *Journal*
548 *of Climate*, 24, 3484–3519, DOI: 10.1175/2011JCLI3955.1 2011.

549 Feng J., J. Quan, H. Liao, Y. Li and X. Zhao: An Air Stagnation Index to Qualify
550 Extreme Haze Events in Northern China. *Journal of the Atmospheric Sciences*, 75,
551 3489-3505. doi:10.1175/JAS-D-17-0354.1. 2018.

552 Fyfe, J. C., Boer, G. J. and Flato, G. M.: The Arctic and Antarctic oscillations and their
553 projected changes under global warming. *Journal of Geophysical Research*, 26,
554 1601–1604, 1999.

555 Griffies S., M. Winton, L. Donner, et al.: The GFDL CM3 Coupled Climate Model:
556 Characteristics of the Ocean and Sea Ice Simulations. *Journal of Climate*, 24(13),
557 3520-3544, 2011.

558 Han Z., B. Zhou, Y. Xu, J. Wu and Y. Shi: Projected changes in haze pollution potential
559 in China: an ensemble of regional climate model simulations. *Atmospheric*
560 *Chemistry and Physics*, 17, 10109–10123. [https://doi.org/10.5194/acp-17-10109-](https://doi.org/10.5194/acp-17-10109-2017)
561 2017, 2017.

562 He J., Gong S., Zhou C. et al.: Analyses of winter circulation types and their impacts
563 on haze pollution in Beijing. *Atmospheric Environment*, 192, 94–103, 2018.

564 Hori, M.E. and Ueda, H.: Impact of global warming on the East Asian winter monsoon
565 as revealed by nine coupled atmosphere-ocean GCMs. *Geophysical Research*
566 *Letters*, 33(3), L03713, 2006.

567 Kobayashi, S., and Coauthors: The JRA-55 reanalysis: general specifications and basic
568 characteristics. *Journal of the Meteorological Society of Japan*, 93(1), 5-
569 48,doi:<http://doi.org/10.2151/jmsj.2015-001>, 2015.

570 Jeong Jaemin I., and Rokjin J. Park: Winter monsoon variability and its impact on aerosol
571 concentrations in East Asia. *Environmental Pollution*, 221, 285e292, 2017.

572 Lamarque J, Bond T, Eyring V, et al.: Historical (1850-2000) gridded anthropogenic
573 and biomass burning emissions of reactive gases and aerosols: Methodology and
574 application, *Atmospheric Chemistry and Physics*, 10, 7017–7039, 2010.

575 Li, Q., Zhang, R., Wang, Y.: Interannual variation of the wintertime fog-haze days
576 across central and eastern China and its relation with East Asian winter monsoon.
577 *International Journal of Climatology*. 36, 346e354, 2016.

578 Li, K., Liao, H., Cai, W., & Yang, Y.: Attribution of anthropogenic influence on
579 atmospheric patterns conducive to recent most severe haze over eastern China.
580 *Geophysical Research Letters*, 45, 2072–2081. [https://doi.org/10.1002/](https://doi.org/10.1002/2017GL076570)
581 [2017GL076570](https://doi.org/10.1002/2017GL076570), 2018.

582 Liu, C., Zhang, F., Miao, L., Lei, Y. & Yang, Q. Future haze events in Beijing, China:
583 When climate warms by 1.5 and 2.0C. *Int. J. Climatol.*, 40, 3689–3700, 2019a.

584 Liu, Z. et al. A Model Investigation of Aerosol Induced Changes in the East Asian
585 Winter Monsoon. *Geophys. Res. Lett.*, 46, 10186–10195, 2019b.

586 Luo F., L. Wilcox, B. Dong et al.: Projected near-term changes of temperature extremes
587 in Europe and China under different aerosol emissions. *Environmental Research*
588 *Letters*, 15,034013, 2020.

589 Ming Y., V. Ramaswamy, L. J. Donner, and V. T. J. Phillips: A robust parameterization
590 of cloud droplet activation. *J. Atmos. Sci.*, 63, 1348–1356, 2006.

591 Niu F., Z. Q. Li, C. Li, K.-H. Lee, and M. Y. Wang: Increase of wintertime fog in China:
592 Potential impacts of weakening of the eastern Asian monsoon circulation and
593 increasing aerosol loading, *J. Geophys. Res.*, 115, D00K20,
594 doi:10.1029/2009JD013484, 2010.

595 Pei L. and Z. W., Yan: Diminishing clear winter skies in Beijing towards a possible
596 future. *Environmental Research Letters*, 13, 124029, 2018.

597 Pei L., Z.W, Yan, Z. Sun, S. Miao, Y. Yao: Increasing persistent haze in Beijing:
598 potential impacts of weakening East Asian winter monsoons associated with
599 northwestern Pacific sea surface temperature trends. *Atmospheric Chemistry and*
600 *Physics*, 18,3173–83, 2018.

601 Pei L., Yan Z.W., Chen D., and Miao S.: Climate variability or anthropogenic emissions:
602 which caused Beijing Haze? *Environmental Research Letters*, 15 034004, 2020.

603 Scannell C., and Coauthors: The Influence of Remote Aerosol Forcing from
604 Industrialized Economies on the Future Evolution of East and West African
605 Rainfall. *Journal of Climate*, 32, 8335–8354, [https://doi.org/10.1175/JCLI-D-18-](https://doi.org/10.1175/JCLI-D-18-0716.1)
606 [0716.1](https://doi.org/10.1175/JCLI-D-18-0716.1). 2019.

607 Shindell D. T., R. L. Miller, G. A. Schmidt, L. Pandolfo: Simulation of recent northern
608 winter climate trends by greenhouse-gas forcing. *Nature*, 399, 452–455, 1999.

609 Taylor K. E., Stouffer B. J., and Meehl, G. A.: An overview of CMIP5 and the
610 experiment design, *Bull. Am. Meteorol. Soc.*, 93, 485–498, 2012.

611 Wang H. J., H. P. Chen, and J. P. Liu: Arctic sea ice decline intensified haze pollution
612 in eastern China, *Atmospheric and Oceanic Science Letters*, 1–9, 2015.

613 Wang L., Chen W.: An intensity index for the east Asian winter monsoon. *Journal of*
614 *Climate*, 27, 2361. <https://dx.doi.org/10.1175/JCLI-D-13-00086.1>, 2014.

615 Wang Y., T. Le, G. Chen, et al.: Reduced European aerosol emissions suppress winter
616 extremes over northern Eurasia. *Nature Climate Change*,10, 225–230, 2020.

- 617 Williams K. D., C. M. Harris, A. Bodas-Salcedo, et al.: The Met office global coupled
618 model 2.0 (GC2) configuration *Geoscientific Model Development*, 8,1509–24,
619 2015.
- 620 Wu P., Y. Ding, Y. Liu: Atmospheric circulation and dynamic mechanism for persistent
621 haze events in the Beijing–Tianjin–Hebei region. *Advances in Atmospheric*
622 *Sciences*, 34, 429–40, doi: 10.1007/s00376-016-6158-z. 2017.
- 623 Zhang R.H., Li, Q., Zhang, R.N.: Meteorological conditions for the persistent severe
624 fog and haze event over eastern China in January. *Science China Earth Sciences*,
625 57, 26–35. <https://doi.org/10.1007/s11430-013-4774-3>, 2014.
- 626 Zhang Y.J., Yin Z.C., Wang H.J.: Roles of climate variability on the rapid increases of
627 early winter haze pollution in North China after 2010. *Atmos. Chem. Phys.*, 20,
628 12211–12221, 2020.
- 629 Zheng B., D. Tong, M. Li, et al: Trends in China’s anthropogenic emissions since 2010
630 as the consequence of clean air actions. *Atmospheric Chemistry and Physics*, 18,
631 14095–111, 2018.
- 632

633 **Figure Captions:**

634 **Fig. 1** Composite circulation anomalies from JRA-55 with HWI-daily>0 (left) and
635 HWI-month \geq 1 (right) for 1958-2013. (a)-(b) temperature anomalies (K) along
636 40°N, (c)-(d) 500hPa winds anomalies (vector, m s⁻¹) and its zonal component
637 (shading, m s⁻¹). (e)-(f) 850hPa winds (vector, m s⁻¹) and its meridional component
638 (shading, m s⁻¹). The green boxes/lines indicate the regions used to calculate the
639 three components of HWI.

640 **Fig.2** Changes in winter HWI from 1958 to 2013 in JRA-55 reanalysis relative to 1958-
641 2013 winter mean. (a) DJF mean monthly-based HWI (HWI-month, black line)
642 and the anomalous days with daily based HWI >0 (HWI-daily, red line, unit: day),
643 (b) scatter plot of HWI-month (y-axis) and the ratio of days with HWI-daily>0 (x-
644 axis) in each winter month. HWI-month and HWI-daily are the HWI calculated
645 from monthly data and daily data, respectively. (c)-(d) are the anomalies of haze
646 occurrence and the VN3day when HWI \geq 1, where VN3day is the minimum 3-day
647 consecutive visibility. Cross area in (c)-(d) is statistically significant at the 10%
648 level using a Student's t-test.

649 **Fig.3** (a) Probability density function (PDF) via a non-parametric density estimation,
650 Kernel density estimation, and (b) cumulative distribution function (CDF)
651 distributions of HWI in winters of His (1980-2004, grey), CLE (2016-2050, blue)
652 and MTFR (2016-2050, pink) simulated by HadGEM3-GC2. (c)-(d) are results for
653 GFDL-CM3. The numbers in (a) and (c) are the climate mean of HWI, and in (b)

654 and (d) are the frequency of month with $HWI \geq 1$, respectively.

655 **Fig.4** Histogram plots for the 2000 bootstrapped samples of (a) changes in winter mean
656 HWI, and (b) frequency with $HWI \geq 1$ in HadGEM3-GC2, and (c)-(d) similarly for
657 GFDL-CM3. The grey, blue and pink shadings are the results estimated from His,
658 CLE and MTFR respectively. Solid (dashed) grey, blue and pink lines are the
659 results of multi-member mean (95% confidence level) in His, CLE and MTFR,
660 respectively.

661 **Fig.5** The difference in winter mean temperature (K) along $40^\circ N$ (left) between CLE
662 (2016-2050) and His (1980-2004), and (right) between MTFR (2016-2050) and
663 CLE (2016-2050). The dotted areas are statistically significant at the 10% level
664 using a Student's t-test. The green lines indicate the level and longitude used in the
665 calculation of ΔT .

666 **Fig.6** Spatial distribution for the difference in winter mean 850 hPa winds (vector, $m s^{-1}$) and
667 850hPa meridional component (shading, $m s^{-1}$) (left) between CLE (2016-
668 2050) and His (1980-2004), and (right) between MTFR (2016-2050) and CLE
669 (2016-2050). The dotted areas denote the 850hPa meridional winds statistically
670 significant at the 10% level using a Student's t-test. The black box indicates the
671 region used in the calculation of V_{850} .

672 **Fig.7** Same as Fig.6, but for the difference in 500hPa winds (vector, $m s^{-1}$) and its zonal
673 component (shading, $m s^{-1}$). The black boxes indicate the regions used in the

674 calculation of U500.

675 **Fig.8** The difference of the climate mean surface temperature (left, K) and sea level
676 pressure (right, hPa) between MTFR and CLE simulated by (a)-(b) HadGEM3-
677 GC2 and (c)-(d) GFDL-CM3. The dotted areas in (a)-(d) are statistically
678 significant at the 10% level using a Student's t-test. PDF via Kernel density
679 estimation of EAWM in His (1980-2004, grey), CLE (2016-2050, blue) and
680 MTFR (2016-2050, pink) simulated by (e) HadGEM3-GC2, and (f) GFDL-CM3.
681 The numbers in (e)-(f) are the climate mean of EAWM.

682 **Fig.9** Winter mean (left) AOD at 550 nm in (a) HadGEM3-GC2 and (c) GFDL-CM3
683 averaged over 1980-2004. Right is same as left, but for the mean AOD_ratio of
684 AOD averaged in the winter months with $HWI \geq 1$ (hereafter AOD_ratio($HWI \geq 1$))
685 in His. Blue and red shadings in (b) and (d) are decreased and elevated AOD
686 relative to the baseline mean, respectively.

687 **Fig.10** Same as Fig.9b and d, but for the results projected in CLE and MTFR. The
688 dotted areas are statistically significant at the 10% level using a Student's t-test.

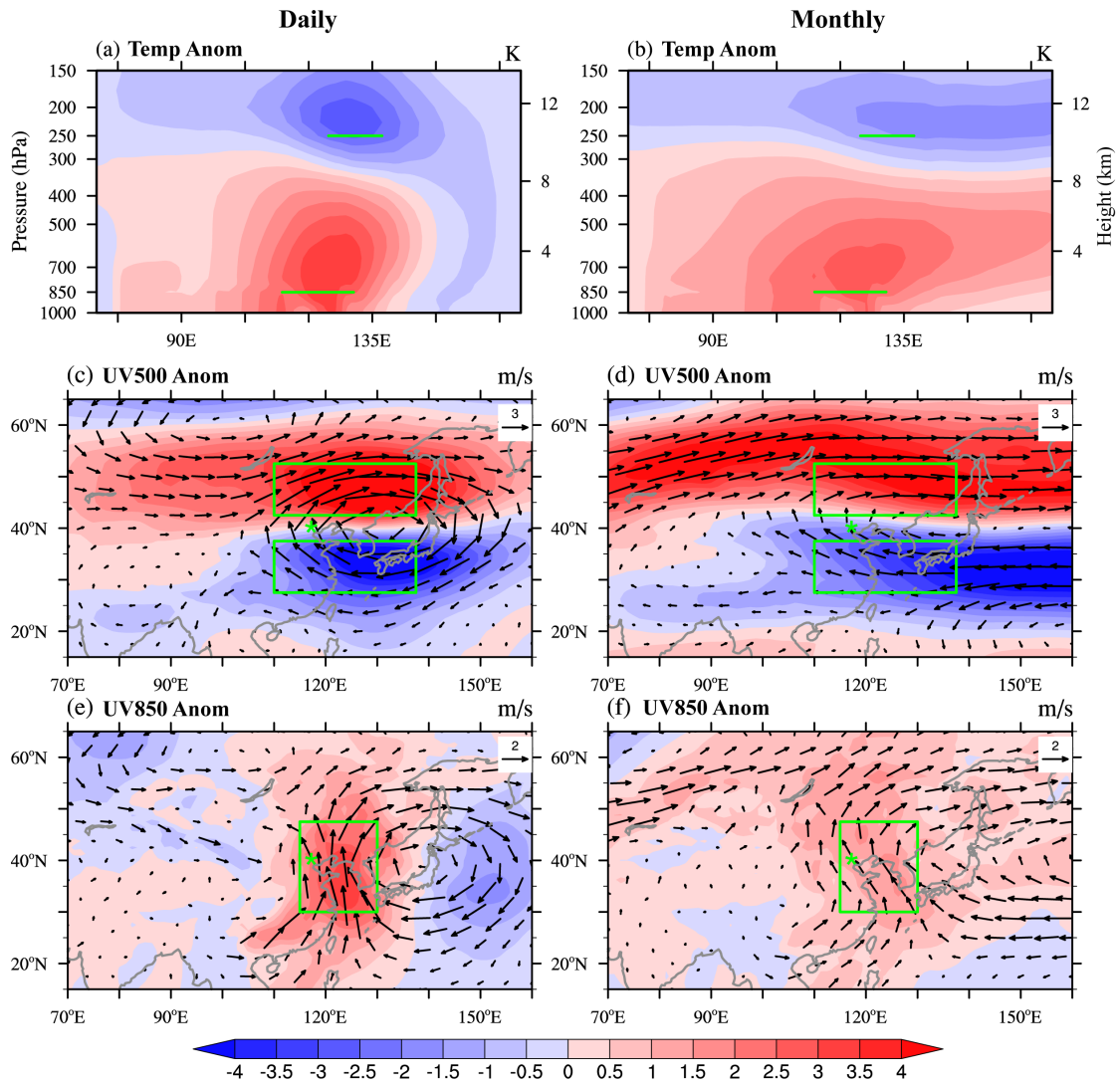
689 **Fig.11** (a) PDF and (b) CDF distributions of AOD_ratio($HWI \geq 1$) over North China
690 (33-45°N, 105-122°E, box in Fig.2) in HadGEM3-GC2. (c)-(d) are the results
691 from GFDL-CM3. The grey, blue and pink vertical lines and numbers in (a) and
692 (c) are the winter mean AOD_ratio($HWI \geq 1$) of His, CLE and MTFR, respectively.
693 The numbers in (b) and (d) are the cumulative probability of AOD_ratio($HWI \geq 1$)

694 higher than the winter mean AOD_ratio($HWI \geq 1$) of His.

695

696

697



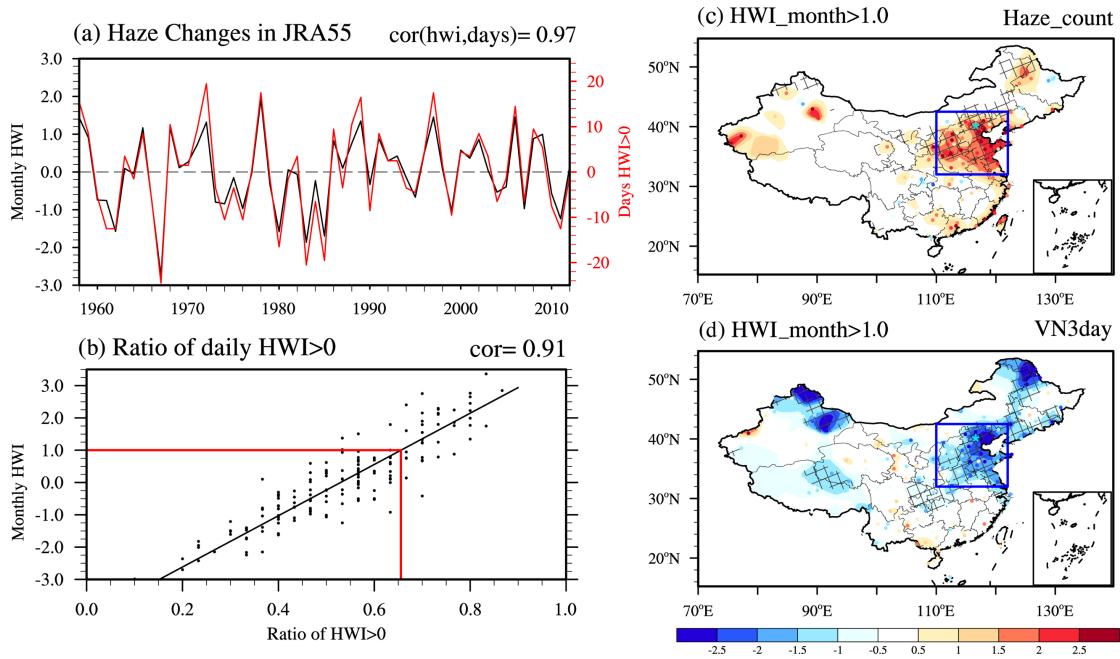
698

699 **Fig. 1** Composite circulation anomalies from JRA-55 with HWI-daily>0 (left) and
 700 HWI-month \geq 1 (right) for 1958-2013. (a)-(b) temperature (K) along 40°N, (c)-(d)
 701 500hPa winds (vector, m s^{-1}) and its zonal component (shading, m s^{-1}). (e)-(f) 850hPa
 702 winds (vector, m s^{-1}) and its meridional component (shading, m s^{-1}). The green
 703 boxes/lines indicate the regions used to calculate the three components of HWI.

704

705

706

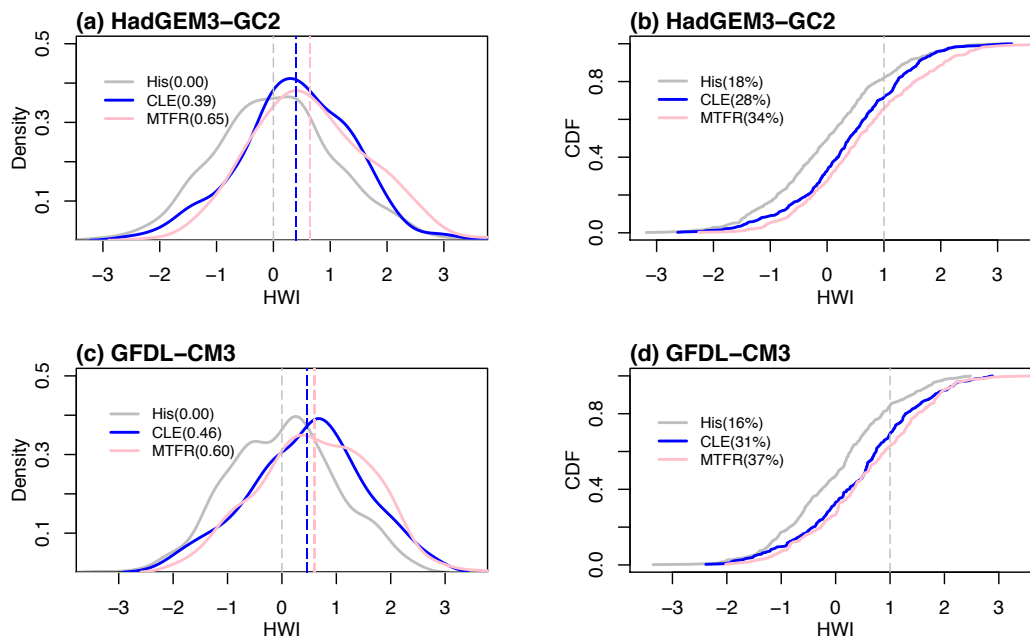


707

708 **Fig.2** Changes in winter HWI from 1958 to 2013 in JRA-55 reanalysis relative to 1958-
 709 2013 winter mean. (a) DJF mean monthly-based HWI (HWI-month, black line) and the
 710 anomalous days with daily based HWI>0 (HWI-daily, red line, unit: day), (b) scatter
 711 plot of HWI-month of December, January and February (y-axis) and the ratio of days
 712 with HWI-daily>0 (x-axis) in each winter month. HWI-month and HWI-daily are the
 713 HWI calculated from monthly data and daily data, respectively. (c)-(d) are the
 714 anomalies of haze occurrence and the VN3day when HWI \geq 1, where VN3day is the
 715 minimum 3-day consecutive visibility. Cross area in (c)-(d) is statistically significant at
 716 the 10% level using a Student's t-test.

717

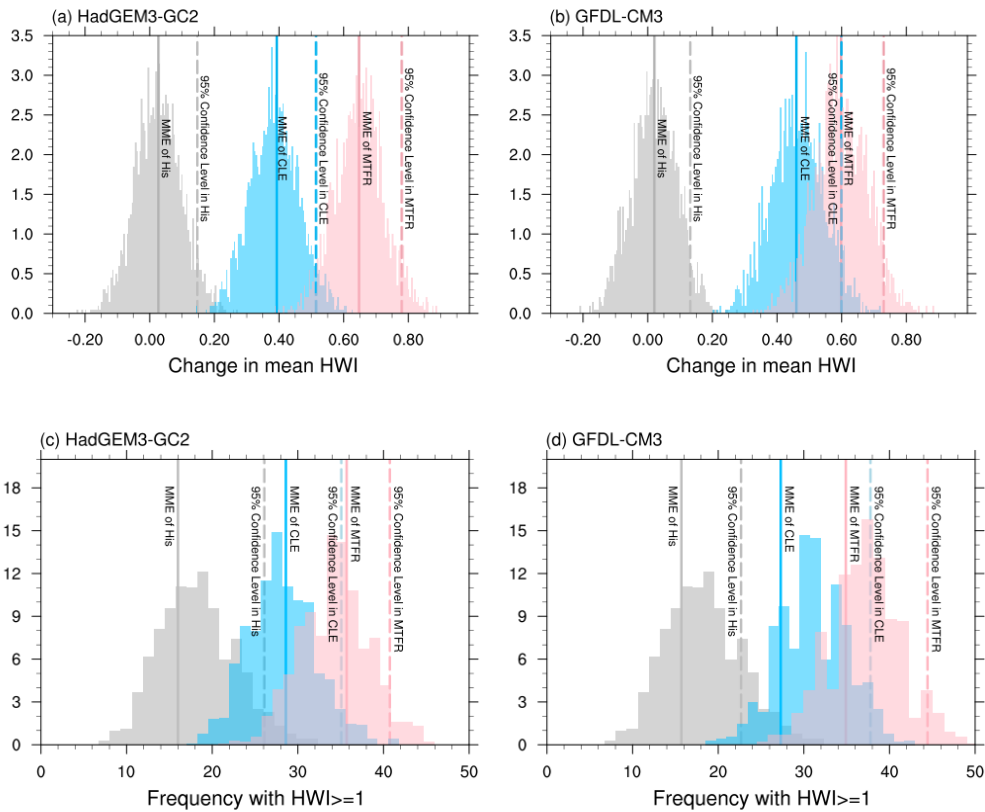
718



720

721 **Fig. 3** (a) Probability density function (PDF) via a non-parametric density estimation,
 722 Kernel density estimation, and (b) cumulative distribution function (CDF) distributions
 723 of HWI in winters of His (1980-2004, grey), CLE (2016-2050, blue) and MTFR (2016-
 724 2050, pink) simulated by HadGEM3-GC2. (c)-(d) are results for GFDL-CM3. The
 725 numbers in (a) and (c) are the climate mean of HWI, and in (b) and (d) are the frequency
 726 of month with HWI ≥ 1 , respectively.

727



728

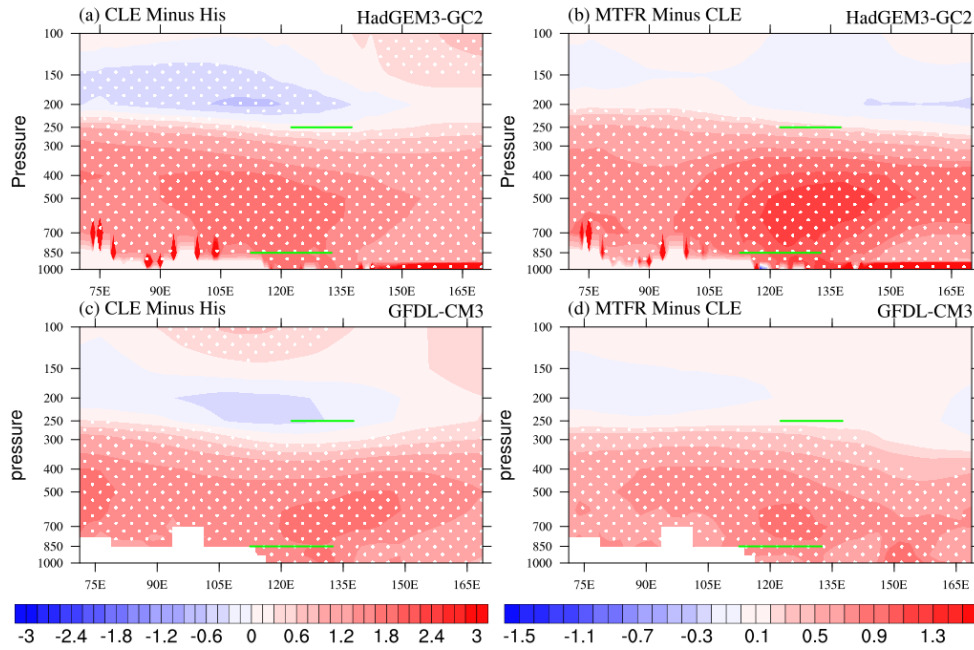
729

730

731 **Fig. 4** Histogram plots for the 2000 bootstrapped samples of (a) changes in winter mean
 732 HWI, and (c) frequency of month with $HWI \geq 1$ in HadGEM3-GC2, and (b), (d)
 733 similarly for GFDL-CM3. The grey, blue and pink shadings are the results estimated
 734 from His, CLE and MTRF respectively. Solid (dashed) grey, blue and pink lines are the
 735 results of multi-member mean (95% confidence level) in His, CLE and MTRF,
 736 respectively.

737

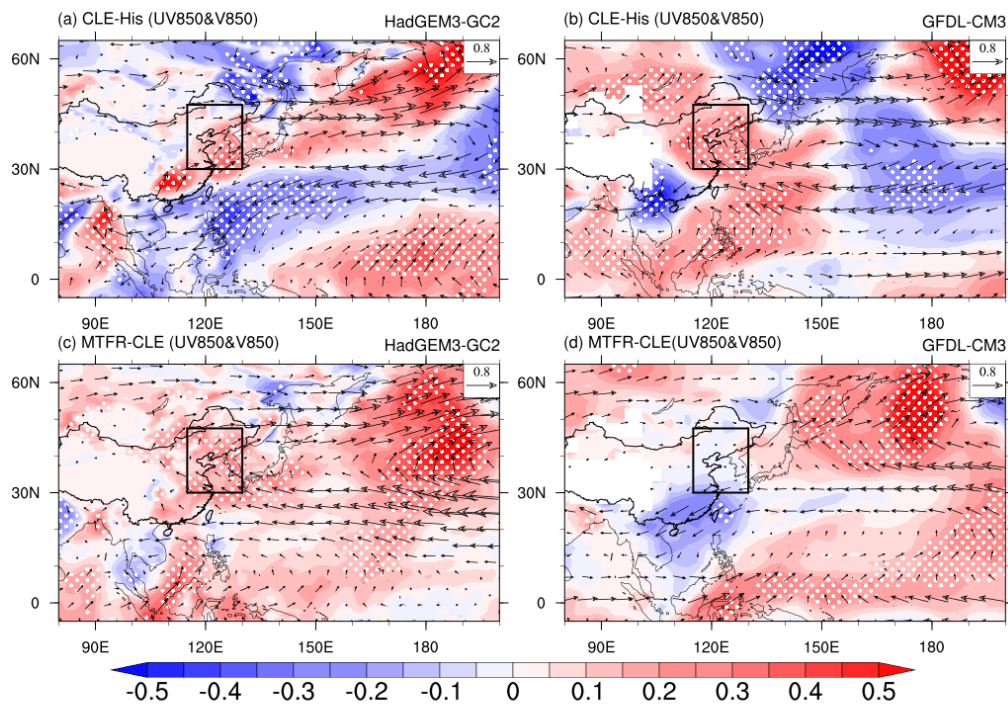
738



739

740 **Fig.5** The difference in winter mean temperature (K) along 40°N (left) between CLE
 741 (2016-2050) and His (1980-2004), and (right) between MTFR (2016-2050) and CLE
 742 (2016-2050). The dotted areas are statistically significant at the 10% level using a
 743 Student's t-test. The green lines indicate the level and longitude used in the calculation
 744 of ΔT .

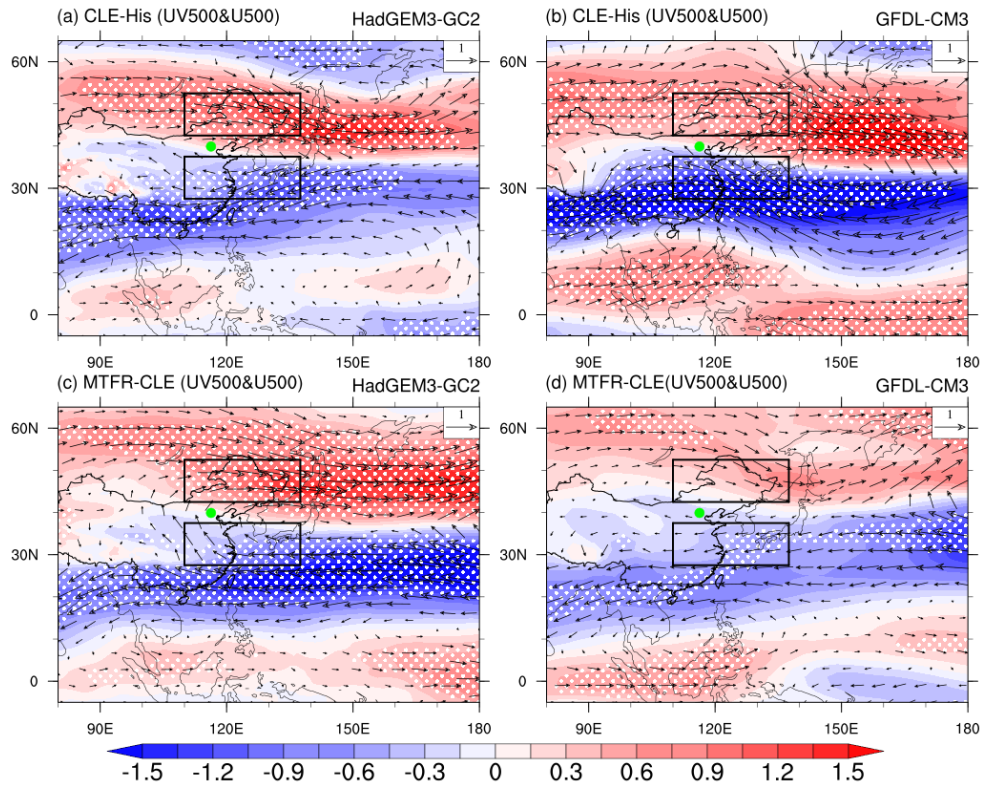
745



747

748 **Fig.6** Spatial distribution for the difference in winter mean 850 hPa winds (vector, m s^{-1}) and 850hPa meridional component (shading, m s^{-1}) (left) between CLE (2016-2050) and His (1980-2004), and (right) between MTFR (2016-2050) and CLE (2016-2050).
 749
 750
 751 The dotted areas denote the 850hPa meridional winds statistically significant at the 10%
 752 level using a Student's t-test. The black box indicates the region used in the calculation
 753 of V850.

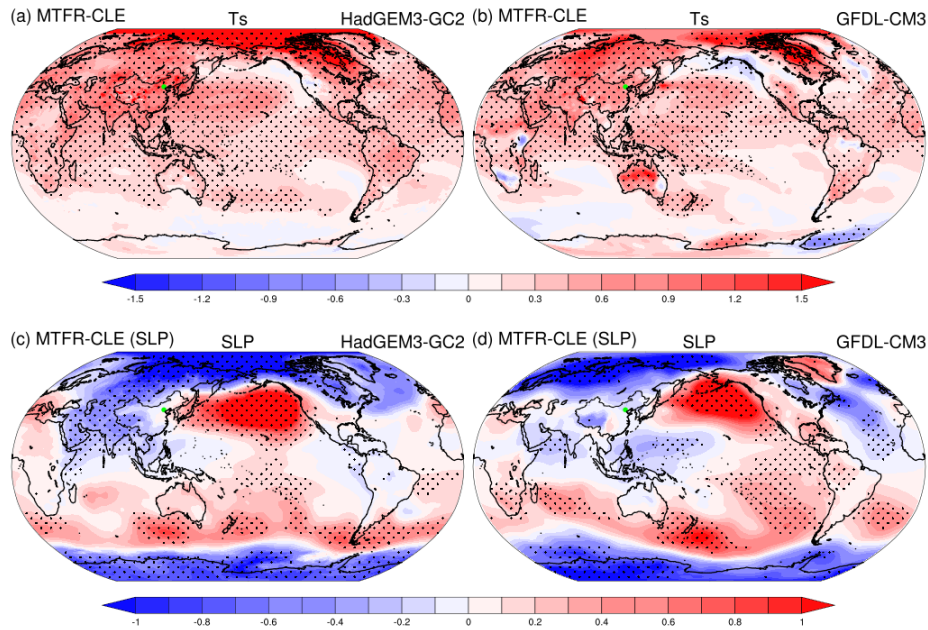
754



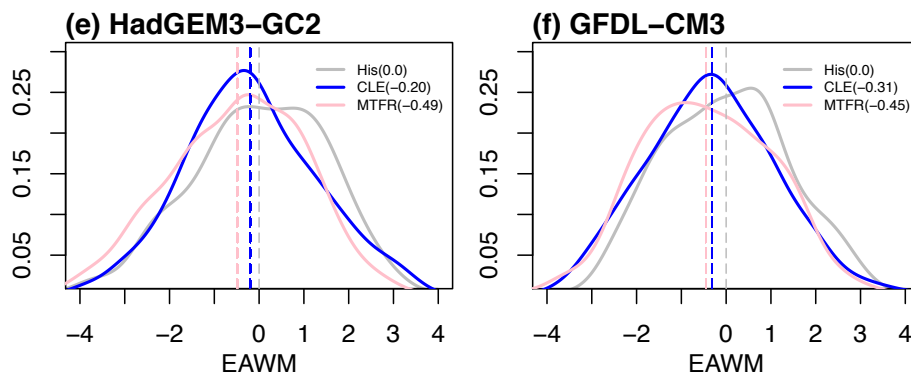
755

756 **Fig.7** Same as Fig.6, but for the difference in 500hPa winds (vector, m s^{-1}) and 500hPa
 757 zonal component (shading, m s^{-1}). The black boxes indicate the regions used in the
 758 calculation of U500.

759



760



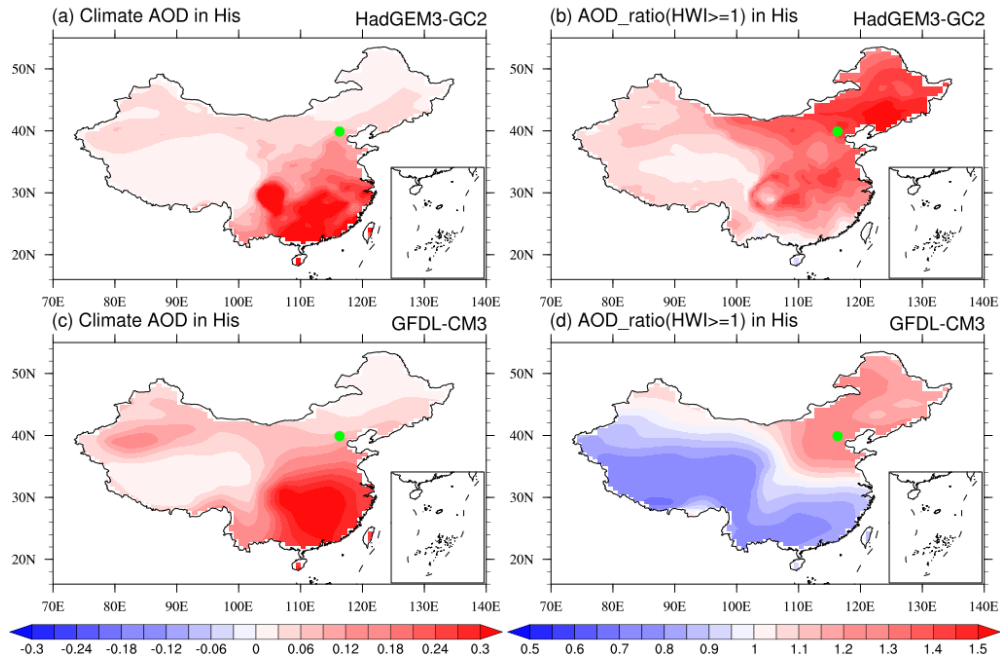
761

762 **Fig.8** The difference of the climate mean surface temperature (left, K) and sea level
 763 pressure (right, hPa) between MTFR and CLE simulated by (a)-(b) HadGEM3-GC2
 764 and (c)-(d) GFDL-CM3. The dotted areas in (a)-(d) are statistically significant at the
 765 10% level using a Student's t-test. PDF via Kernel density estimation of EAWM in His
 766 (1980-2004, grey), CLE (2016-2050, blue) and MTFR (2016-2050, pink) simulated by
 767 (e) HadGEM3-GC2, and (f) GFDL-CM3. The numbers in (e)-(f) are the climate mean
 768 of EAWM.

769

770

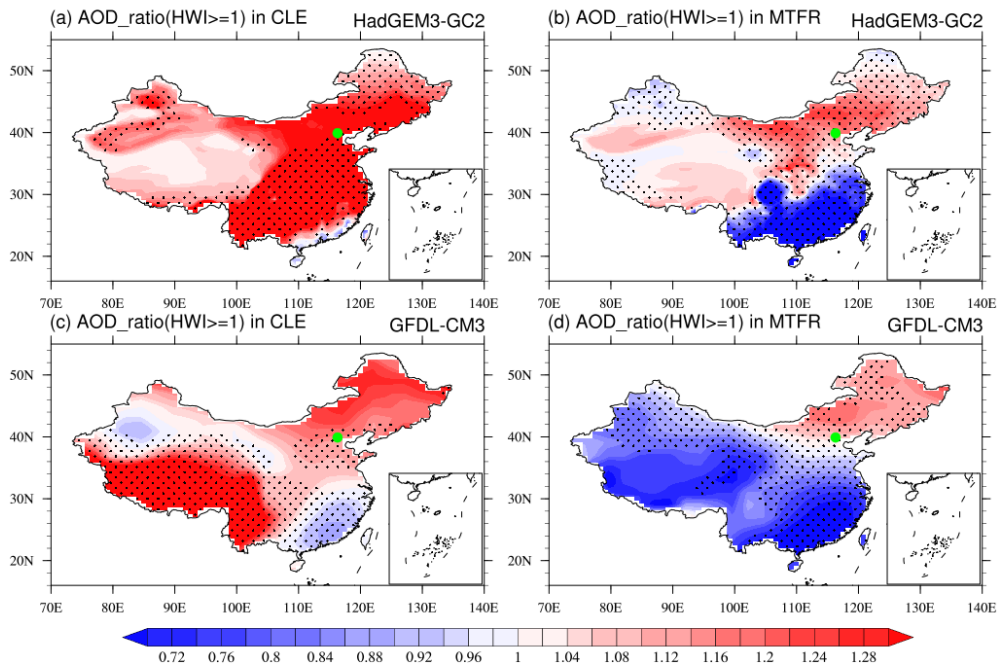
771



772

773 **Fig.9** Winter mean (left) AOD at 550 nm in (a) HadGEM3-GC2 and (c) GFDL-CM3
 774 averaged over 1980-2004. Right is same as left, but for the mean AOD_ratio in the
 775 winter months with $HWI \geq 1$ (hereafter AOD_ratio($HWI \geq 1$)) in His. Blue and red
 776 shadings in (b) and (d) are decreased and elevated AOD relative to the climate winter
 777 mean of His, respectively.

778



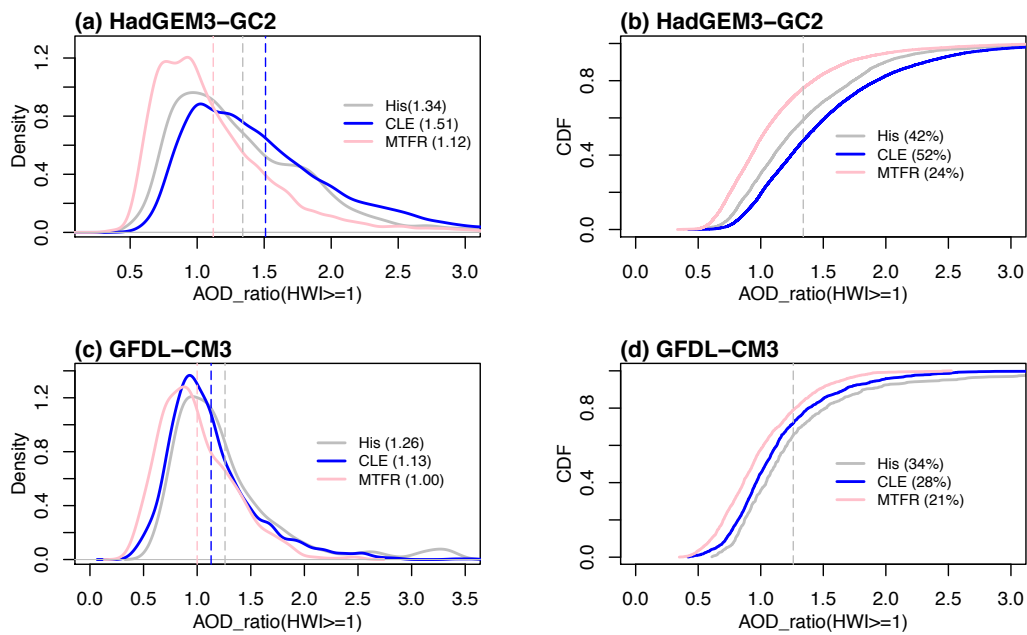
779

780 **Fig 10.** Same as Fig.9b and d, but for the results projected in CLE and MTFR. The

781 dotted areas are statistically significant at the 10% level using a Student's t-test.

782

783



784

785 **Fig.11** (a) PDF and (b) CDF distributions of AOD_ratio(HWI ≥ 1) over North China
 786 (33-45°N, 105-122°E, box in Fig.2) in HadGEM3-GC2. (c)-(d) are the results from
 787 GFDL-CM3. The grey, blue and pink vertical lines and numbers in (a) and (c) are the
 788 winter mean AOD_ratio(HWI ≥ 1) of His, CLE and MTFR, respectively. The numbers
 789 in (b) and (d) are the cumulative probability of AOD_ratio(HWI ≥ 1) higher than the
 790 winter mean AOD_ratio(HWI ≥ 1) of His.